Single-cell *Tsc1* knockout during corticogenesis generates tuber-like lesions and reduces seizure threshold in mice

David M. Feliciano, Tiffany Su, Jean Lopez, Jean-Claude Platel, and Angélique Bordey

Departments of Neurosurgery, and Cellular and Molecular Physiology, Yale University School of Medicine, New Haven, Connecticut, USA.

Tuberous sclerosis complex (TSC) is an autosomal dominant disorder characterized by mutations in *Tsc1* or *Tsc2* that lead to mammalian target of rapamycin (mTOR) hyperactivity. Patients with TSC suffer from intractable seizures resulting from cortical malformations known as tubers, but research into how these tubers form has been limited because of the lack of an animal model. To address this limitation, we used in utero electroporation to knock out *Tsc1* in selected neuronal populations in mice heterozygous for a mutant *Tsc1* allele that eliminates the *Tsc1* gene product at a precise developmental time point. Knockout of *Tsc1* in single cells led to increased mTOR activity and soma size in the affected neurons. The mice exhibited white matter heterotopic nodules and discrete cortical tuber-like lesions containing cytomegalic and multinucleated neurons with abnormal dendritic trees resembling giant cells. Cortical tubers in the mutant mice did not exhibit signs of gliosis. Furthermore, phospho-S6 immunoreactivity was not upregulated in *Tsc1*-null astrocytes despite a lower seizure threshold. Collectively, these data suggest that a double-hit strategy to eliminate *Tsc1* in discrete neuronal populations generates TSC-associated cortical lesions, providing a model to uncover the mechanisms of lesion formation and cortical hyperexcitability. In addition, the absence of glial reactivity argues against a contribution of astrocytes to lesion-associated hyperexcitability.

Introduction

Tuberous sclerosis complex (TSC) is an autosomal dominant disorder that causes lesions in many different organs including in the brain, skin, heart, and kidney. The incidence of TSC is estimated between 1:6,000 and 1:10,000 individuals (1). TSC is caused by mutations in 1 of 2 tumor suppressor genes, *TSC1* and *TSC2*, which encode hamartin and tuberin, respectively, and lead to hyperactivity of mammalian target of rapamycin (mTOR) (2). Although TSC affects many organ systems, the neurological symptoms causing the most significant disability and morbidity include seizures, mental retardation, and autism. Epilepsy is observed in more than 80% of affected individuals, and seizures often begin during the first year of life as infantile spasms that are unresponsive to conventional anti-epileptic drug therapies (3–6).

Seizures in TSC individuals are associated with cortical lesions or malformations called tubers (7). Indeed, seizures have a focal or multifocal origin with a topographic correspondence between EEG foci and MRI high-signal lesions, demonstrating the preponderant role of cortical tubers as epileptogenic foci (8, 9). Resecting tubers in pharmacologically intractable epileptic patients with TSC reduces or eliminates seizure activity in a subpopulation of these patients (8, 10). However, how a tuber forms and contributes to cortical hyperexcitability remains unclear in the absence of a reliable animal model of cortical tubers.

One animal model of cortical tubers is the Eker rat, which has a germline mutation in the *Tsc2* gene (11–13). However, the low incidence of the tubers (1 in 14 rats) clearly argues for developing a new animal model of cortical tubers. No tubers have been reported in heterozygote *Tsc1* or *Tsc2* mice that express a mutant allele (14–17). Recent evidence indicates that tubers form by biallelic *TSC1* or *TSC2* gene inactivation, reflecting a double-hit mechanism of germline and somatic mutational events likely occurring during development (18). However, this remains debated, as second-hit point mutations are not a common event in tubers and were not detected in another recent study (19). Irradiation of neonatal Eker rats led to cortical lesions resembling cortical tubers (20), but whether biallelic inactivation and mTOR hyperactivity occurred was unknown. Conditional (floxed) *Tsc1* and *Tsc2* transgenic mice have thus been generated and crossed with Cre lines, inducing gene deletion at specific times during development (21–23). While this strategy mimics some of the TSC brain alterations seen in humans (e.g., seizures, enlarged and dysplastic cortical neurons), these models do not replicate the focal nature of the tubers and the associated heterotopic nodules. The cortex of TSC individuals contains pockets of abnormal cells with hyperactive mTOR in an otherwise structurally normal brain (24–28).

To generate discrete TSC-like lesions, we propose a double-hit strategy in transgenic mice carrying conditional and mutant (mut) *Tsc1* alleles by deleting the conditional *Tsc1* allele in embryonic progenitor cells using in utero electroporation. These $Tsc1^{fl/mut}$ mice were generated by crossing $Tsc1^{fl/fl}$ with $Tsc1^{WT/mut}$ (17, 29). Using a floxed strategy combined with in utero electroporation led to the formation of tuber-like lesions and heterotopic nodules in the cortex, leading to lower seizure threshold. One unexpected finding was the lack of gliosis and the absence of mTOR hyperactivity in $Tsc1^{null}$ astrocytes in the cortical lesions. Overall, the present strategy has the power to address critical questions related to the molecular pathogenesis and the etiology of TSC lesions.

Results

In utero single-cell genetic deletion of Tsc1 using a Cre-Lox system. We used in utero electroporation to express Cre recombinase (Cre) and remove *Tsc1* in $Tsc1^{fl/WT}$ and $Tsc1^{fl/mut}$ embryos (Figure 1). Consid-

Conflict of interest: The authors have declared that no conflict of interest exists.

Citation for this article: *J Clin Invest.* 2011;121(4):1596–1607. doi:10.1172/JCI44909.

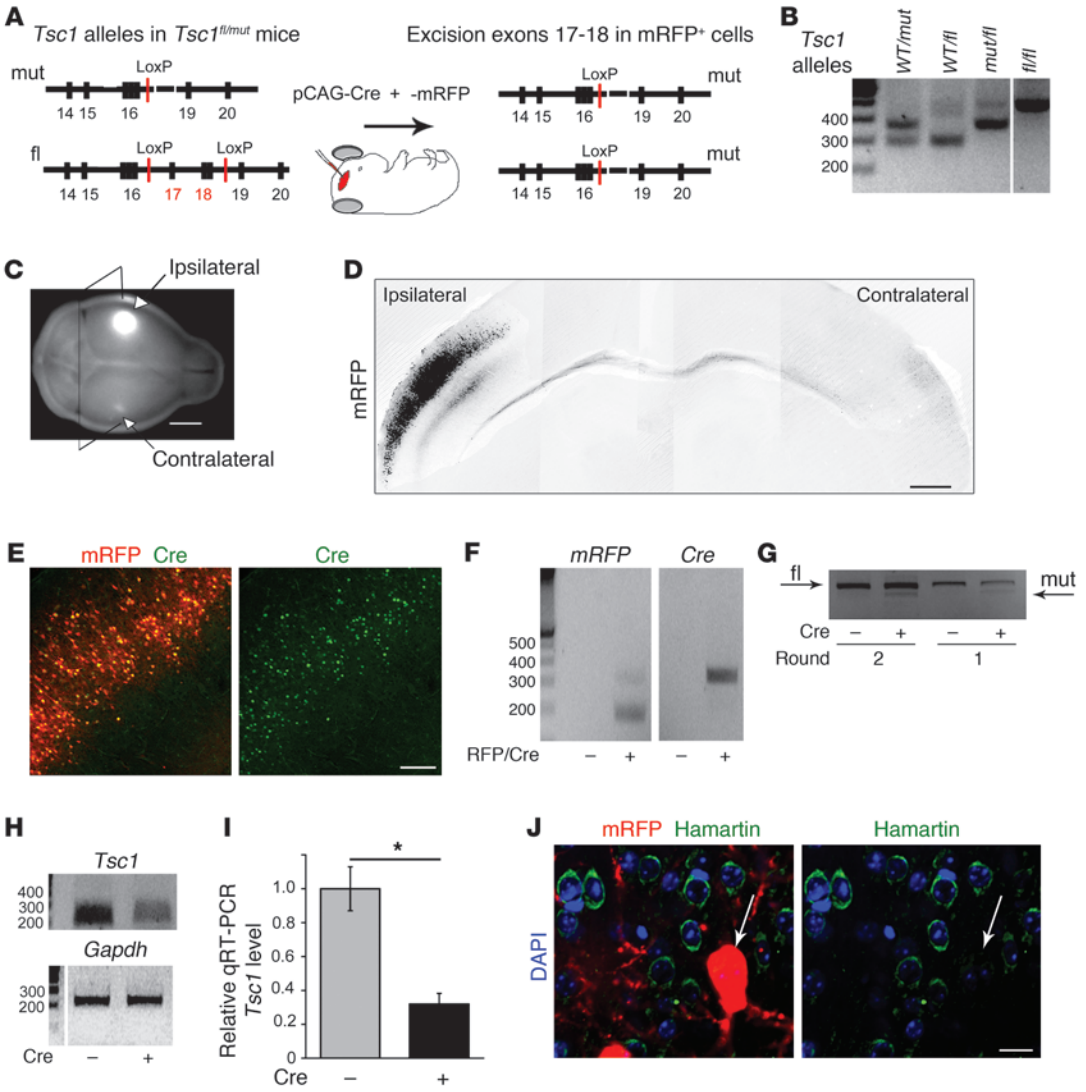

Figure 1

In utero single-cell knockout of *Tsc1* in cortical cells. (**A**) Exons/introns of mutant and floxed alleles before and after Cre-induced excisions of exons 17–18 in the floxed allele. (**B**) PCR gels of genomic DNA from the mouse lines. (**C**) P28-fixed brains containing a cortical area electroporated with mRFP. Fluorescent projections from the ipsilateral side containing mRFP$^+$ cells are visible. (**D**) Coronal section containing electroporated mRFP$^+$ cells in the ipsilateral side sent projections to the contralateral cortex from a P15 *Tsc1*$^{fl/WT}$ mouse electroporated at E15. Shown is a composite of several images. (**E**) mRFP$^+$ (red) and Cre:GFP$^+$ (green) cells in cortex of a P15 *Tsc1*$^{fl/WT}$ mouse electroporated at E15. (**F**) PCR gels of DNA plasmid for mRFP and Cre extracted from microdissected mRFP$^+$ cell–containing cortex and contralateral cortex in P7 *Tsc1*$^{fl/mut}$ mice. (**G**) PCR gels from genomic DNA obtained from ipsilateral (mRFP-containing cells) and contralateral cortical tissue microdissected from slices obtained from a P28 *Tsc1*$^{fl/fl}$ mouse electroporated at E16. (**H**) PCR gels of Tsc1 and Gapdh cDNA obtained from ipsilateral and contralateral P7 *Tsc1*$^{fl/mut}$ cortex. (**I**) Relative abundance of *Tsc1* mRNA measured by qRT-PCR and obtained from ipsilateral (mRFP-containing cells) and contralateral cortical tissue microdissected from slices obtained from a P28 *Tsc1*$^{fl/mut}$ mouse electroporated at E16. *$P < 0.005$. (**J**) Hamartin immunostaining (green), mRFP fluorescence (red), and DAPI nuclear counterstain (blue) in ipsilateral cortex from a P28 *Tsc1*$^{fl/mut}$ mouse electroporated at E15. Arrows indicate the mRFP$^+$ cell that stained negative for hamartin (green). Scale bars: 3 mm (**C**), 350 μm (**D**), 140 μm (**E**), 30 μm (**J**). Lanes in **B** and **H** were run on the same gel but were noncontiguous (white lines).

ering that individuals with TSC are born with a systemic loss of one *Tsc1* (or *Tsc2*) allele, we compared data obtained from *Tsc1*$^{fl/mut}$ mice with those obtained from littermate *Tsc1*$^{fl/WT}$ mice. The *Tsc1*^{fl} allele contains LoxP sites surrounding the sequence to be excised upon Cre recombination (Figure 1A). The *Tsc1*^{mut} allele is similar to a recombined allele and contributes to a frame shift and truncated transcript, rendering TSC1 (i.e., hamartin) nonfunctional. Figure 1B illustrates the PCR gels for the genotyping of the different mouse lines. A combination of primers was used to detect the WT (at 295 bp), floxed (at 480 bp), and mutant *Tsc1* alleles (at 370 bp).

A combination of pCAG-cre:GFP (Cre fused to GFP) and pCAG-mRFP were electroporated at E15–E16. The fluorescence of the monomeric red fluorescent protein (mRFP) plasmid was visible by eye on dissected brains. Photographs of the fixed brains using

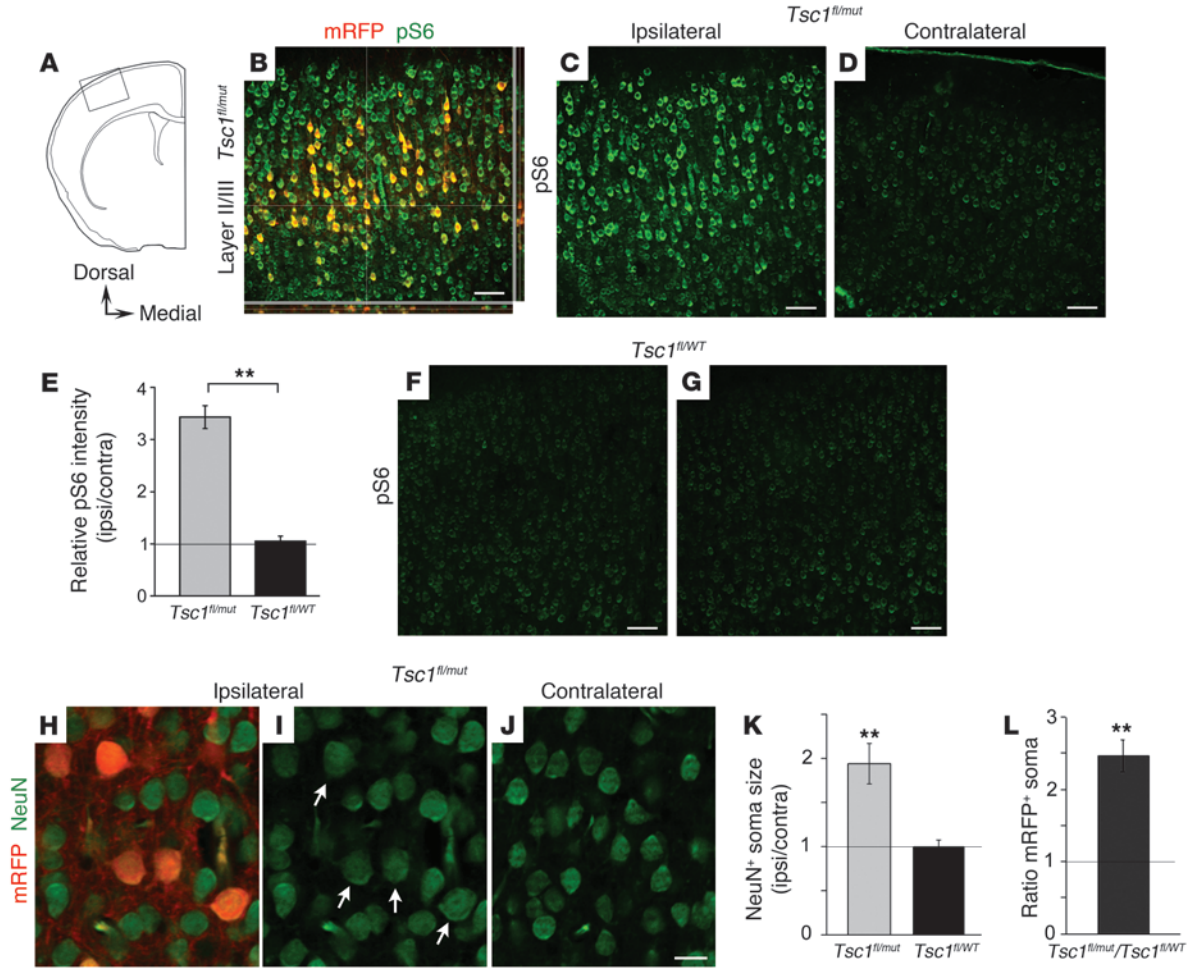

Figure 2

Single-cell *Tsc1* deletion increases mTOR activity and cell size in *Tsc1*$^{fl/mut}$ mice. (**A**) Diagram of a coronal section illustrating the cortical ROI. (**B**) pS6 immunostaining (green) in the ipsilateral mRFP$^+$ cell–containing cortex from a P15 *Tsc1*$^{fl/mut}$ mouse electroporated at E16. (**C**, **D**, **F**, and **G**) pS6 (Ser240/244) immunostaining in the ipsilateral and contralateral cortex from P15 *Tsc1*$^{fl/mut}$ (**C** and **D**) and *Tsc1*$^{fl/WT}$ mice (**F** and **G**) electroporated at E16. (**E**) Bar graphs of the ratio of pS6 intensity in the ipsilateral versus contralateral cortical layer II/III from *Tsc1*$^{fl/mut}$ mice ($n = 9$) and *Tsc1*$^{fl/WT}$ mice ($n = 6$, P15 and P28 pooled). $^{**}P < 0.005$. (**H**–**J**) NeuN immunostaining (green) in the ipsilateral mRFP$^+$ cell–containing cortex (**H** and **I**; **I** does not show the red channel) and the contralateral cortex (**J**) from a P15 *Tsc1*$^{fl/mut}$ electroporated at E16. (**K**) Bar graph of ipsilateral/contralateral NeuN$^+$ soma size in cortical layer II/III from *Tsc1*$^{fl/mut}$ ($n = 8$) and *Tsc1*$^{fl/WT}$ mice ($n = 5$, P15 and P28 pooled). $^{**}P < 0.005$. (**L**) Bar graph of the ratio of mRFP$^+$ soma size in the *Tsc1*$^{fl/mut}$ versus *Tsc1*$^{fl/WT}$ cortical layer II/III ($n = 6$ and 5 mice, respectively). $^{**}P < 0.005$. Scale bars: 70 μm (**B**–**D**, **F**, and **G**) and 15 μm (**H**–**J**).

a sensitive fluorescent illumination and detection system illustrate both the area of the cortex containing mRFP$^+$ cells and the contralateral area containing mRFP$^+$ projections (Figure 1C). Such ipsilateral and contralateral areas were clearly visible on confocal photographs obtained on coronal brain sections (Figure 1D). In addition, a dual fluorescence from GFP and mRFP was visible (Figure 1E). The vector encoding cre:GFP had a nuclear localization sequence, which resulted in nuclear GFP expression, while mRFP was distributed throughout the cell cytoplasm. Both Cre and mRFP DNA were also detected using PCR from the ipsilateral (i.e., electroporated) but not the contralateral cortex microdissected from P7 brains electroporated at E15 (Figure 1F). Next, to determine whether recombination occurred at the *Tsc1*^{fl} alleles, we prepared genomic DNA from microdissected ipsilateral and contralateral cortical layer II/III obtained from P28 *Tsc1*$^{fl/fl}$ mice electroporated at E15. We found a *Tsc1* mutant allele band from the ipsilateral tissue but not from the contralateral tissue, suggesting that recombination had occurred, leading to *Tsc1* removal in electroporated cells (Figure 1G).

Finally, we examined *Tsc1* mRNA and protein expression. RT-PCR for *Tsc1* illustrated that there was a significant decrease in *Tsc1* but not *Gapdh* mRNA in the ipsilateral compared with the contralateral P7 cortex (Figure 1G). To better quantify the loss of *Tsc1*, we performed quantitative RT-PCR (qRT-PCR). *Tsc1* mRNA levels were decreased by 70% in the ipsilateral compared with the contralateral cortex microdissected from P28 *Tsc1*$^{fl/mut}$ mice electroporated at E16 ($n = 5$ or 6 samples each from 2 mice; Figure 1I). There was not a complete loss, due to contamination of non-electroporated cells in the microdissected cortex. Immunostaining for hamartin in E15-electroporated P28 *Tsc1*$^{fl/mut}$ mice revealed that all mRFP$^+$ cells exam-

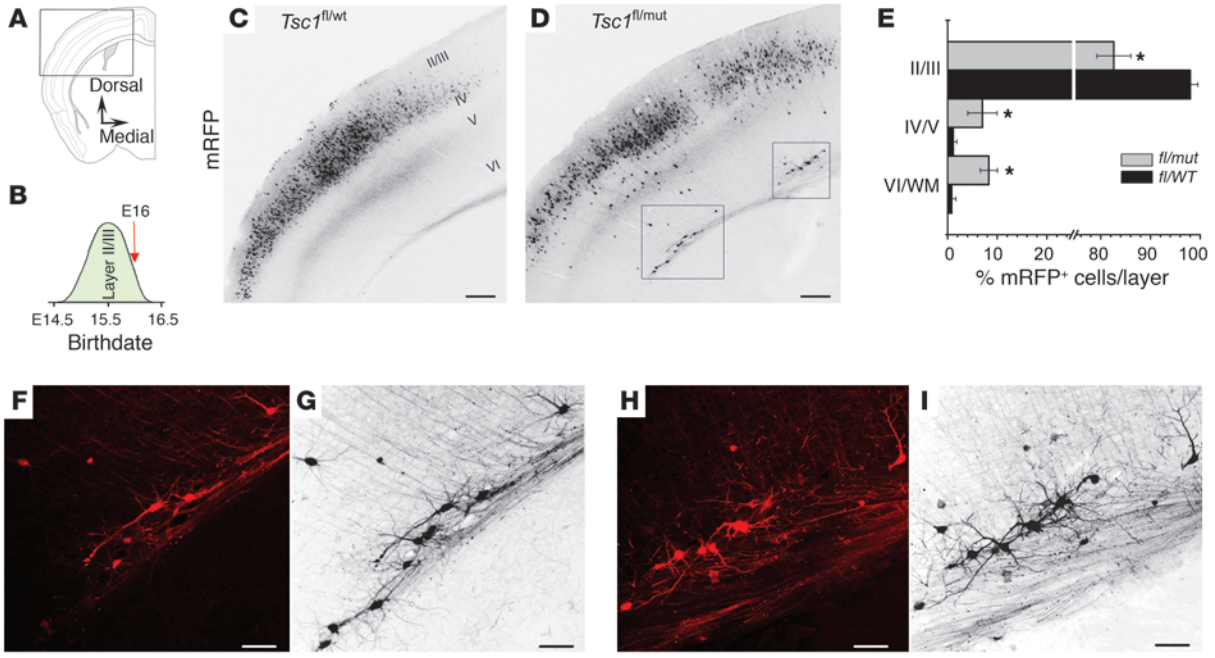

Figure 3

Heterotopic nodule formation with cytomegalic neurons after electroporation at E16. (**A**) Diagram of a coronal section illustrating the cortical ROI. (**B**) Diagram illustrating the approximate birthdate of cortical layer II/III neurons. The red arrow indicates the time of electroporation at E16. (**C** and **D**) Photographs of mRFP$^+$ cells in the somato-sensory cortex in coronal sections from P15 *Tsc1*$^{fl/WT}$ (**C**) and *Tsc1*$^{fl/mut}$ mice (**D**) electroporated at E16. (**E**) Bar graphs illustrating the distribution (as a percentage) of mRFP$^+$ cells across cortical layers in *Tsc1*$^{fl/WT}$ and *Tsc1*$^{fl/mut}$ mice. WM, white matter. *$P < 0.05$. (**F**–**I**) Confocal images of mRFP$^+$ cells in one optical section (red, **F** and **H**) and a Z-stack (19.5 μm, black, **G** and **I**) from the boxed regions in **D**. Scale bars: 140 μm (**C** and **D**) and 70 μm (**F**–**I**).

ined displayed no hamartin staining, while surrounding mRFP$^-$ cells displayed cytoplasmic hamartin staining ($n = 3$ mice; Figure 1J). In addition, mRFP$^+$ cells in E15-electroporated P28 *Tsc1*$^{fl/WT}$ mice also displayed hamartin staining (data not shown).

Collectively, these data suggest that in utero electroporation is a reliable method to excise floxed *Tsc1* allele(s) upon Cre expression that results in knockout and haploinsufficiency of *Tsc1* in mRFP$^+$ cells from *Tsc1*$^{fl/mut}$ and *Tsc1*$^{fl/WT}$ mice (hereafter referred to as *Tsc1*^{null} and *Tsc1*^{haplo} cells), respectively.

Single-cell Tsc1 deletion results in increased mTOR activity and cell size. The *TSC1* gene product, hamartin, negatively regulates mTOR activity, which controls S6 phosphorylation. Phospho-S6 (pS6) is thus commonly used as a marker of mTOR activity. Immunostaining for pS6 (Ser240/244) in E16-electroporated *Tsc1*$^{fl/mut}$ mice revealed that mRFP$^+$ neurons displayed a 3.4-fold elevation in intensity of pS6 staining compared with mRFP$^-$ neurons in the contralateral side ($n = 9$ mice; $P < 0.01$; Figure 2, A–E, E15 and E16 electroporation combined). In Figure 2B, mRFP$^-$ neurons in the ipsilateral side also displayed enhanced pS6 compared with neurons in the contralateral side (Figure 2D). This resulted from dilution of the mRFP-encoding plasmid compared with genomic *Tsc1* removal (see below). In contrast, loss of a single *Tsc1* allele in mRFP$^+$ cells of *Tsc1*$^{fl/WT}$ mice did not increase pS6 ($n = 6$ mice; Figure 2, E–G). As a result, the ratio of pS6 staining in *Tsc1*^{null} cells from *Tsc1*$^{fl/mut}$ mice was significantly higher than that in *Tsc1*^{haplo} cells from *Tsc1*$^{fl/WT}$ mice (Figure 2E).

mTOR hyperactivity leads to increased cell size in other cell types. We thus quantified the soma size of layer II/III mRFP$^+$ and contralateral mRFP$^-$ neurons using NeuN immunostaining. In *Tsc1*$^{fl/mut}$ mice, the mean soma size of NeuN$^+$/mRFP$^+$ neurons was significantly larger than that of mRFP$^-$ neurons in the contralateral cortex ($P < 0.01$, $n = 8$ mice; Figure 2, H–K). As shown for pS6, loss of a single allele in mRFP$^+$ cells of *Tsc1*$^{fl/WT}$ mice did not result in increased cell size ($n = 5$ mice; Figure 2K). In addition, measuring the soma of mRFP$^+$ cells in slices from *Tsc1*$^{fl/mut}$ and *Tsc1*$^{fl/WT}$ mice revealed that *Tsc1*^{null} neurons had a significantly larger soma than *Tsc1*^{haplo} neurons ($n = 6$ and 5 mice, respectively, 93% increase; Figure 2L).

These data suggest that the mTOR pathway was hyperactivated in mRFP$^+$ cells in *Tsc1*$^{fl/mut}$ mice (i.e., *Tsc1*^{null} cells) upon knockout of *Tsc1*. In addition, loss of heterozygosity using a double-hit strategy resulted in larger mTOR hyperactivity and cell size increase than loss of only a single allele.

Formation of heterotopic nodules with cytomegalic neurons in Tsc1$^{fl/mut}$ *mice*. Considering the increased mTOR activity in *Tsc1*^{null} cells, we examined sections for the presence of malformations in the neocortex following electroporation at E16 (Figure 3, A–D). E16 is close to the end of layer II/III neurogenesis in the neocortex of WT mice (ref. 30 and Figure 3B). While 98% ± 1% of *Tsc1*^{haplo} cells reached layer II/III, 17% ± 3% of *Tsc1*^{null} cells were misplaced ($n = 3$ mice; $P < 0.05$; Figure 3, C–E). In particular, electroporated *Tsc1*$^{fl/mut}$ cortex displayed misplaced groups of cells, called heterotopic nodules, in layer VI/subplate and in the white matter (Figure 3D). mRFP$^+$ cells in the nodules and in layer II/III were all NeuN$^+$ and were thus identified as neurons (data not shown). Heterotopic nodules contained 5–25 neurons. These *Tsc1*^{null} neurons in the nodules exhibited enlarged soma size (93% increase

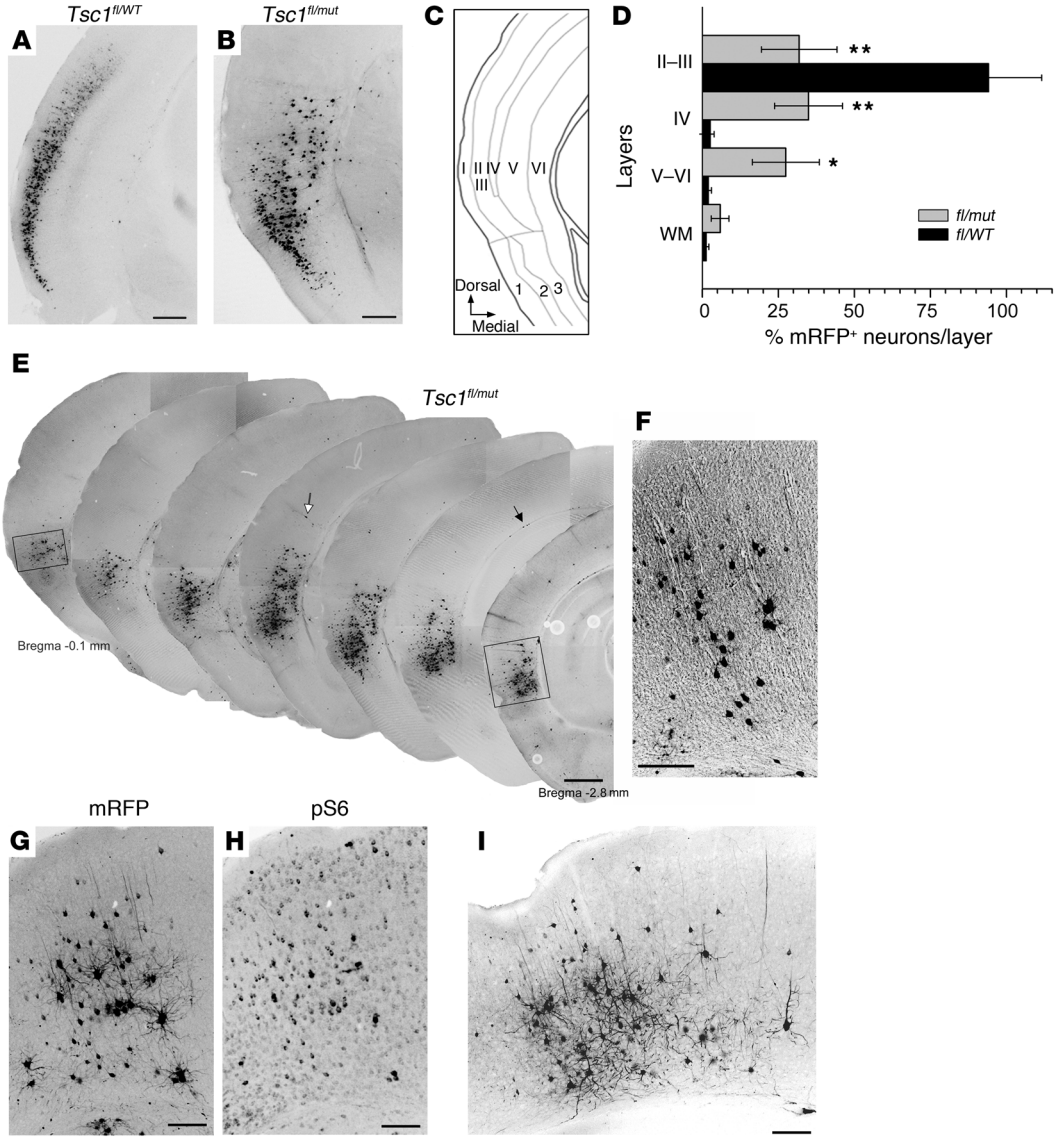

Figure 4

Single-cell *Tsc1* deletion at E15 generates tuber-like lesions in *Tsc1*$^{fl/mut}$ mice. (**A** and **B**) Photographs of mRFP$^+$ cells in P28 coronal sections from *Tsc1*$^{fl/WT}$ (**A**) and *Tsc1*$^{fl/mut}$ mice (**B**) electroporated at the onset of layer II/III birth (E15). (**C**) Diagram of a coronal section illustrating the cortical ROI and the regions of the cortex, consisting of 6, 5, or 3 layers. (**D**) Bar graphs illustrating the distribution (as a percentage) of mRFP$^+$ cells across cortical layers in *Tsc1*$^{fl/WT}$ ($n = 7$) and *Tsc1*$^{fl/mut}$ mice ($n = 4$). *$P < 0.05$; **$P < 0.005$. (**E**) Photographs of mRFP$^+$ cells in P28 serial coronal sections (bregma –0.08 to –2.8 mm) from a *Tsc1*$^{fl/WT}$ mouse electroporated at E15. The black arrows point to scattered white matter cells; white arrow points to a small group of mRFP$^+$ cells. (**F**) Photograph of mRFP$^+$ cells on a DIC image in the rectangle from the most rostral section in **E**, illustrating a radial column of migration. (**G** and **H**) pS6 immunostaining and corresponding mRFP$^+$ cells in a coronal section from a P28 *Tsc1*$^{fl/mut}$ mouse. (**I**) Photograph of mRFP$^+$ cells in the rectangle of the most caudal section in **E**. Scale bars: 300 μm (**A**, **B**, and **E**), 100 μm (**F**), 70 μm (**G** and **H**), and 140 μm (**I**). Images are from mice electroporated at E15.

compared with *Tsc1*^{null} neurons in layer II/III) and a dysplastic morphology (Figure 3, F–I).

Collectively, these data suggest that single-cell *Tsc1* deletion at the end of layer II/III neurogenesis leads to the formation of heterotopic nodules with cytomegalic neurons in and above the white matter that resemble white matter heterotopia seen in TSC individuals. Nevertheless, approximately 80% of the mRFP$^+$ cells reached the proper layer. We hypothesized that only 20% of the cells were affected because of the time necessary to produce Cre following electroporation and for hamartin to be degraded (half-life of ~24 hours; ref. 31). We thus examined whether electroporation at E15, corresponding to the onset of layer II/III formation, would generate larger lesions.

Single-cell Tsc1 deletion at E15 generates tuber-like lesions in Tsc1$^{fl/mut}$ *mice.* Electroporation at E15 is expected to affect a greater proportion of layer II/III–predetermined neurons, the generation of which starts at approximately E14.5 (30, 32). Following E15 electroporation, a simple visual inspection of P28 slices was sufficient

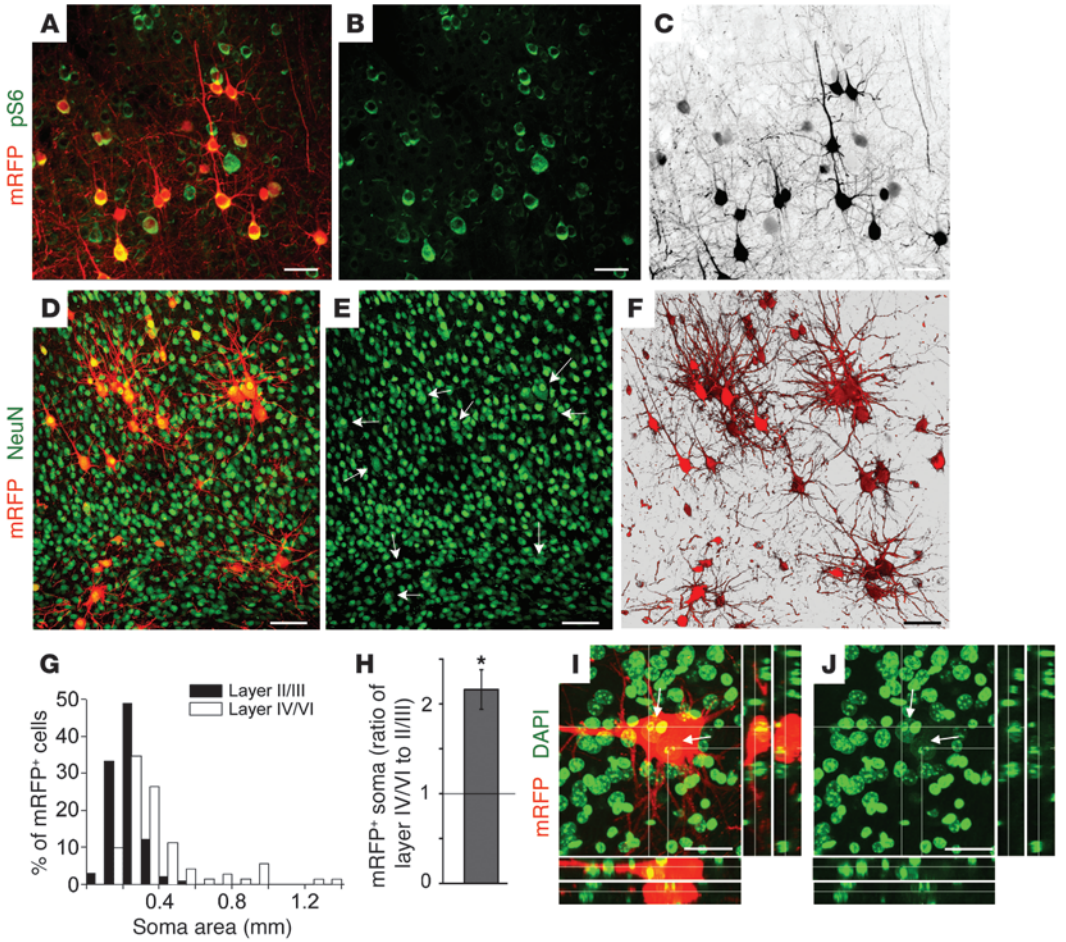

Figure 5

pS6+ enlarged cells are neuronal, dysmorphic, and multinucleated. (**A** and **B**) Confocal photographs of mRFP+ cells (red) and pS6 immunostaining (green) in cortical layer V–VI. (**C**) Black and white image of the red fluorescence in **A**, illustrating the mosaic nature of cell sizes. (**D** and **E**) Confocal photographs of mRFP+ cells (red) and NeuN (green) immunostaining overlay in cortical layer V (**E** does not show the red channel). Arrows in **E** denote electroporated cells, which colocalized with NeuN staining. (**G**) Histogram of cell area in upper and deeper layers in cortical sections from *Tsc1*$^{fl/mut}$ mice. (**H**) Bar graph of the ratio of the soma area of mRFP+ cells in layers IV/VI versus II/III in *Tsc1*$^{fl/mut}$ mice. *$P < 0.005$. (**I** and **J**) Confocal Z-stack photographs and projections of an mRFP+ cell (red) and DAPI (pseudo-colored green) in layer VI. All the images are from P28 *Tsc1*$^{fl/mut}$ mice electroporated at E15. Scale bars: 70 μm (**A**–**C**), 40 μm (**D**–**F**), 50 μm (**I** and **J**).

to observe striking misplacement of *Tsc1*^{null} neurons compared with *Tsc1*^{haplo} neurons (in *Tsc1*$^{fl/mut}$ versus *Tsc1*$^{fl/WT}$ mice, respectively; Figure 4, A and B). The majority of *Tsc1*^{haplo} neurons (94%) were localized to layers II/III, as expected ($n = 7$ *Tsc1*$^{fl/WT}$ mice). By contrast, 68% of *Tsc1*^{null} neurons were misplaced throughout layers IV–VI, leading to a loss of lamination ($n = 4$ *Tsc1*$^{fl/mut}$ mice; Figure 4, B–D). The lesion displayed in Figure 4B spanned different cortices in the dorso-ventral axis, from a 6-layer, to a 5-layer, to a 3-layer cortex (piriform cortex). The most dramatically affected cortex was the 6-layer cortex.

Serial sectioning revealed that the lesions spanned about 3 mm, and this size was controlled by the electroporation span (Figure 1C and Figure 4E). Despite a rostro-caudal neurogenic gradient, the lesion was prominent at every level. Nevertheless, the limbic cortex was significantly more affected than the piriform cortex in terms of cell misplacement, giving an appearance of 2 distinct lesions. Finally, cell scattering through the white matter (black arrows in Figure 4E) was visible in all of the sections. The rostral tail of the lesions displayed misplaced cells in a columnar organization reminiscent of a radial migratory track (Figure 4F).

Pathologically in humans, cortical tubers are characterized by a focal loss of normal cortical architecture, with prominent giant cells that have enlarged nuclei and soma, high pS6 levels, and a dysmorphic arborization (24–28). Examination of the cortical lesions in *Tsc1*$^{fl/mut}$ mice revealed the presence of cytomegalic cells scattered throughout layers IV to VI (Figure 4G and Figure 5, A–C). Immunostaining for pS6 was more intense in enlarged and misplaced cells than in surrounding cells (Figure 4H), giving a mosaic appearance of the cortex in terms of pS6 staining and cell size, as seen in individuals with TSC (27). Such a cortical appearance with pS6 staining is routinely used to characterize cortical tubers at the pathological level. In addition, these enlarged cells had a dysmorphic morphology (Figure 4, G and I, and Figure 5).

Another key hallmark of cortical tubers is increased pS6 in giant cells, which are often multinucleated (25, 33). All ectopic cells displayed high pS6 intensity, suggesting mTOR hyperactivity

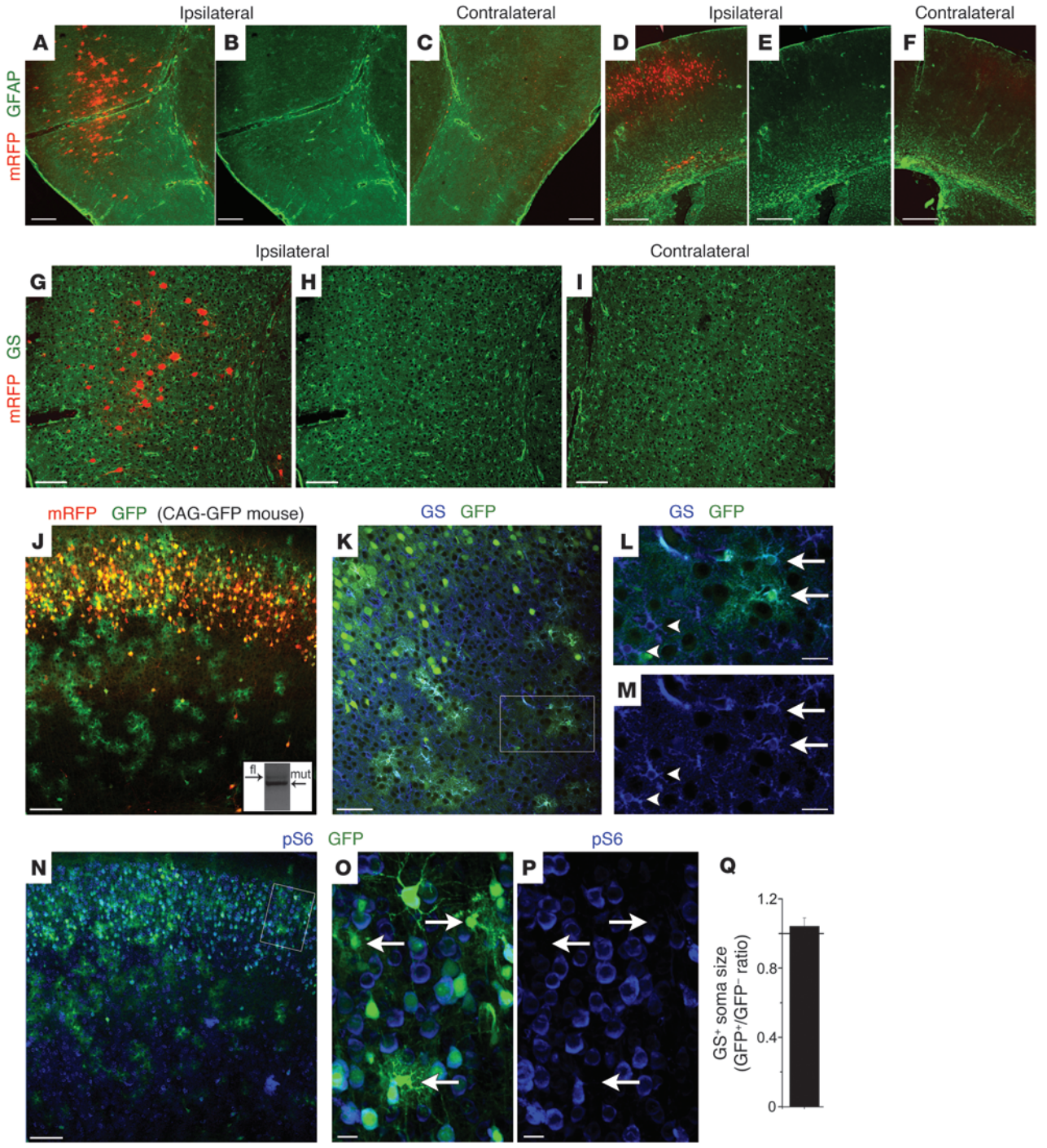

Figure 6

Lack of astrogliosis in the tuber-like lesions. (**A**–**F**) Photograph of mRFP$^+$ cells (red) and GFAP immunostaining (green) in the ipsilateral (**A**, **B**, **D**, and **E**) and contralateral (**C** and **F**) in P28 and P15 *Tsc1*$^{fl/mut}$ mice electroporated at E15 (**A**–**C**) and E16 (**D**–**F**), respectively. (**G**–**I**) Photograph of mRFP$^+$ cells (red) and GS (green) immunostaining in the ipsilateral (**G** and **H**) and contralateral (**I**) in P28 *Tsc1*$^{fl/mut}$ mice electroporated at E15. (**J** and **K**) Photograph of mRFP fluorescence (red, **J**), GS (blue, **K**), and GFP fluorescence (green) in a P15 CAG-GFP × *Tsc1*$^{fl/mut}$ mouse electroporated with pCAG-mRFP and pCAG-Cre:GFP at E16. Inset in **J** shows PCR gels from genomic DNA obtained from E16-electroporated cortical tissue containing electroporated astrocytes but no electroporated neurons, microdissected from slices obtained from a P28 *Tsc1*$^{fl/fl}$ mouse in which no mRFP$^+$ neurons were visible. (**L** and **M**) Higher-magnification photographs of GS staining and GFP fluorescence from the boxed region in **K**. Arrows indicate GFP$^+$ astrocytes (i.e., GS$^+$), and arrowheads indicate GFP$^-$ astrocytes that exhibit the same soma size. (**N**) Photograph of GFP fluorescence (green) and pS6 immunostaining (blue) in a CAG-GFP × *Tsc1*$^{fl/mut}$ mouse electroporated at E16. (**O** and **P**) Higher-magnification photographs of pS6 staining in GFP$^+$ cells from the boxed region in **N**. Arrows point to GFP$^+$ astrocytes that are pS6 negative. (**Q**) Quantification of *Tsc1*$^{fl/mut}$ and *Tsc1*$^{fl/WT}$ astrocytic soma size, as outlined by GS staining. Scale bars: 300 μm (**A**–**F**), 140 μm (**G**–**I**), 70 μm (**J**, **K**, and **N**), 20 μm (**L**, **M**, **O**, and **P**).

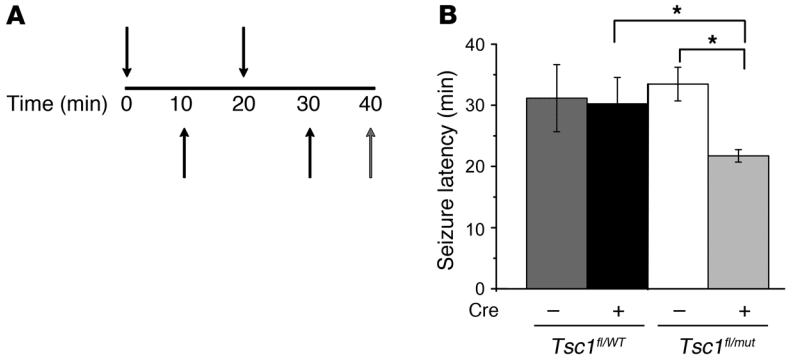

Figure 7
Tsc1$^{fl/mut}$ mice with lesions exhibit a lower seizure threshold. (**A**) Diagram illustrating the protocol of pentylenetetrazole injections. (**B**) Seizure latency in electroporated and non-electroporated P15 *Tsc1*$^{fl/WT}$ and *Tsc1*$^{fl/mut}$ mice. *$P < 0.05$.

(Figure 5, A–C). In addition, ectopic cells were all NeuN$^+$, identifying them as neurons (Figure 5, D–F). They did not express markers of proliferation (Ki67), immature cells (nestin), or immature neurons (doublecortin) (data not shown). Consistent with mTOR hyperactivity, the histogram of soma area and the ratio of soma areas in layer IV/VI versus II/III illustrate that ectopic neurons have a significantly larger soma size than layer II/III neurons ($n = 4$ mice; Figure 5, G and H). In addition, these also illustrate the large distribution of soma sizes for misplaced cells. Finally, about 10% of the enlarged cells were multinucleated with enlarged nuclei compared with surrounding cells in all mice examined (Figure 5, I and J, and Supplemental Figure 1; available online with this article; doi:10.1172/JCI44909DS1). No mRFP$^+$ cells were multinucleated in any of the *Tsc1*$^{fl/WT}$ mice examined ($n = 3$; data not shown).

Collectively, these data suggest that single-cell *Tsc1* deletion leads to the formation of focal cortical lesions with hallmarks of cortical tubers, as seen in individuals with TSC. These lesions in *Tsc1*$^{fl/mut}$ mice are thus referred to as tuber-like lesions.

Lack of astroglial reactivity in tuber-like lesions despite lower seizure threshold. Gliosis or astrogliosis is routinely observed in cortical tubers from individuals with TSC (34). We determined the presence of gliosis using immunostaining for glial fibrillary acidic protein (GFAP). We found no detectable increase in GFAP immunoreactivity in cortical tissue from *Tsc1*$^{fl/mut}$ mice with cortical tuber-like lesions or heterotopic nodules (Figure 6, A–F). We also immunostained for glutamine synthetase (GS), the expression of which is downregulated in TSC astrocytes and reactive astrocytes associated with other epilepsy disorders (34, 35). We found no detectable decrease in GS immunoreactivity in tuber-like lesions (Figure 6, G–I). These data suggest that cortical astrocytes do not react to the presence of tubers or heterotopic nodules.

Astrocytes with enhanced GFAP and loss of GS in individuals with TSC have been reported to express enhanced pS6 staining and enlarged soma size, possibly as a result of *Tsc1* loss (34). In our sections, all mRFP$^+$ cells were NeuN$^+$ and thus neurons. One may presume that astrocytes surrounding the ectopic *Tsc1*^{null} neurons do not change because they have not lost *Tsc1*. However, considering that radial glia transform into astrocytes by the end of neurogenesis, genetic removal of *Tsc1* at the genomic level using the floxed strategy should also lead to *Tsc1* removal in cortical astrocytes. In addition, the mRFP reporter plasmid is expected to be diluted due to successive cell divisions and therefore is not expressed in the last generated cells. We thus crossed *Tsc1*$^{fl/mut}$ mice with CAG-GFP fluorescent reporter mice to induce genomic GFP expression in every Cre-containing cell and compare the expression of GFP fluorescence to that of mRFP fluorescence. mRFP was not observed in GFP$^+$ astrocytes exhibiting an astroglial morphology (Figure 6J), suggesting that mRFP was indeed diluted, while GFP was permanently expressed. These stellar GFP$^+$ cells were identified as astrocytes by GS immunostaining (Figure 6, K–M).

Surprisingly, stellate GFP$^+$ cells, and hence *Tsc1*^{null} astrocytes, did not exhibit increased pS6 immunoreactivity compared with surrounding *Tsc1*^{null} neurons (Figure 6, N–P). Similarly, *Tsc1*^{null} astrocytes were the same size as control astrocytes as determined by GS staining ($n = 3$ mice; Figure 6Q). To determine whether recombination occurred in astrocytes, we microdissected the electroporated cortex from P28 *Tsc1*$^{fl/fl}$ (E16 electroporation) in a region where electroporated neurons were absent (layer IV). We found a *Tsc1* mutant allele band from the ipsilateral tissue (inset of Figure 6J), suggesting that recombination had occurred, leading to *Tsc1* removal in GFP$^+$ astrocytes. These data show that cortical control and *Tsc1*^{null} astrocytes do not react to the presence of heterotopic nodules and tuber-like lesions.

Because gliosis has been proposed to be responsible for cortical hyperexcitability in TSC (34, 36), we examined whether *Tsc1*$^{fl/mut}$ mice containing lesions exhibited a lower seizure threshold. Mice were injected with increasing doses of PTZ (a $GABA_A$ receptor antagonist), and the latency for generalized tonic-clonic seizures was measured. There was a 25% reduction in seizure latency in *Tsc1*$^{fl/mut}$ mice containing heterotopic nodules compared with control littermate *Tsc1*$^{fl/WT}$ mice (Figure 7, A and B). These data suggest that lowered seizure threshold in *Tsc1*$^{fl/mut}$ mice results from the presence of the cortical malformation.

Discussion

Our findings argue that biallelic inactivation of *Tsc1* in cortical neural progenitor cells is necessary for generating malformations resembling cortical tubers and white matter nodules in mice, as seen in TSC patients. In addition, one unexpected finding was the absence of astroglial reactivity and mTOR hyperactivity in *Tsc1*^{null} astrocytes surrounding the lesions despite a reduced seizure threshold.

The cortical malformations described here recapitulate several key features of the TSC-associated brain lesions in humans. These features include loss of lamination, mosaicism of pS6 expression and cell size, and the presence of ectopic cytomegalic neurons (24–28). In the lesion, the presence of pS6$^+$ and multinucleated cytomegalic neurons with a dysmorphic morphology distinguishes TSC-associated lesions from other cortical malformations (37).

However, our model does not replicate all features of human tubers (i.e., spontaneous seizure activity or neurological phenotype, giant cells and astrogliosis). Regarding the lack of seizure activity, it is important to emphasize that although almost all

patients have seizures, not all tubers are epileptogenic (38–40). In fact, as mentioned below the absence of seizures will allow us to increase cell excitability to examine the outcome on gliosis and inflammation observed in human tubers (41). In addition, it remains speculative whether the tubers contribute to neurological phenotypes such as autistic traits (42–44), and we did not examine neurological phenotype past 1 month.

At the cellular level, our lesion lacks cytomegalic cells with a mixed neuron-glial or immature phenotype (e.g., immunostaining for nestin or proliferative markers) called giant cells (25, 26, 28, 33, 45). The absence of such cells could result from the innate differences between human and murine neural progenitor cells. Remarkably, none of the rodent models have reported giant cells (12, 21, 23, 46, 47), although these models have recombination in most of the forebrain instead of a section of the cortex, as shown here. The lack of giant cells here and in other models raises the issue of human and rodent difference. Indeed, the developing human neocortex displays an additional population of proliferative radial glia-like cells in the outer subventricular zone that may contribute to the generation of giant cells with mixed phenotypes in humans (48, 49).

Finally, the lesions were not associated with astrogliosis, as shown by the lack of GFAP upregulation despite *Tsc1* removal in cortical astrocytes. In addition, *Tsc1* removal in astrocytes did not result in a detectable decrease of GS (a functional hallmark of astrogliosis), an elevation of mTOR activity, or a change in cell size. This was unexpected, considering that astrocytes in human tubers show increased GFAP immunoreactivity and cell size and loss of GS (28, 34). We did not explore other features such as K^+ channel and glutamate transporter expression that are altered in epileptic astrocytes or $Tsc1^{null}$ astrocytes (36, 50–52). However, human tubers, which have variable degrees of gliosis, are removed from patients who undergo surgical treatment for focal epilepsy mapped to the resected tubers (53). It is unknown whether tubers not associated with seizures have gliosis (38). Regarding another mouse model of TSC, in which *Tsc2* was removed in the majority of radial glia and cortical mislamination was reported, Way et al. reported that GFAP upregulation was observed in the neocortex (23). However, these mice had spontaneous clinical seizures, which makes comparison difficult with our data because GFAP upregulation and gliosis might result from the seizure activity (see, for example, ref. 54). In a model by Meikle et al., in which *Tsc1* was removed from developing neurons, there was prominent mislamination and increased neuronal size and pS6, but no gliosis (lack of GFAP upregulation) (22). In this model, astrocytes retain *Tsc1* but do not react to the lesion, at least prior to the onset of seizures. Similarly in our model, astrocytes lost *Tsc1* but did not react to the lesion, as shown by the lack of GFAP upregulation. These findings, including ours, raise an important question of whether GFAP upregulation is downstream of the seizure activity. Our model may help to address this question. Indeed, it would be possible to induce either global seizure activity or focal hyperexcitability of tuber neurons through channelrhodopsin-2 (ChR2) (55) or genetically engineered Gq-coupled receptors (56) in vivo and then examine glial reactivity at different time points. ChR2 or genetically engineered Gq-coupled receptors would not be expressed in astrocytes as a result of plasmid dilution that would result in selective neuronal expression and thus neuronal stimulation.

Collectively, our model replicates most of the hallmarks of tubers, including mislamination and ectopic and cytomegalic neurons with high pS6 intermingled with normal-looking cells that have low pS6 but lack the giant cells with mixed phenotype. For this reason, we refer to our lesions as tuber-like. The issue of astrogliosis raises an important question that our model may help address, as mentioned above.

Our approach has several advantages over previous models. One major advantage of our approach is to allow for a precise spatial-temporal inactivation of *Tsc1* and thus the formation of discrete lesions that have not been generated with other TSC models (14, 21–23, 26). In addition, our approach allowed for Tsc1 removal in both neurons and astrocytes and allowed us to precisely choose the timing of recombination by electroporating at different time points from E12 to E18. Compared with other studies, our approach includes the following applications: first, plasmids encoding interference RNA, overexpression system, firefly luciferase for in vivo imaging (ChR2) (55), or engineered Gq-coupled receptors (56) for stimulating tuber-like neurons in slice or in vivo can be co-expressed via electroporation. Second, the tissue surrounding the tuber-like lesion can be studied. This is important because the normal-appearing perituberal tissue has been shown in one study to be the initiation site for epileptiform activity (38). Third, cell migration of $Tsc1^{null}$ neurons in a $Tsc1^{fl/mut}$ cortex can be examined when using fluorescent reporter mice. Using fluorescent rather than LacZ reporter mice is helpful for detecting fluorescence without staining and for future experiments aimed at performing live studies, such as migration assays and patch clamp and calcium experiments. Finally, axonal projections of abnormal neurons can be tracked and their impact on the contralateral neuronal activity can be assessed.

Our data address and raise questions related to the pathogenesis of TSC. First, our data show that biallelic inactivation of *Tsc1* (loss of heterozygosity), which has recently been found in tuber cells (18), is necessary for generating tuber-like lesions. Our findings also support the notion that a double-hit strategy to eliminate functional TSC1 leads to tuber formation. In addition, unpublished observations obtained by comparing data in $Tsc1^{fl/fl}$ versus $Tsc1^{fl/mut}$ mice suggest that a double-hit strategy is required for lesion formation. Second, our approach is based on the assumption that tubers are clonal. In a recent article by Crino and colleagues (18), only a single mutation was found from a pool of tuber cells, suggesting that tubers are clonal. This finding also implies that a neural progenitor cell was affected, leading to the generation of multiple cells with similar mutations, as discussed by others (27, 57). However, there are limited data on the clonality of tubers and no data in humans related to the original cell type affected. Third, temporal targeting of the Cre-containing vector reveals that the earlier *Tsc1* deletion occurs, the more dramatic is the malformation in terms of size and mislamination. The spatial targeting to different cortices also led to differently sized or mislayered malformations when comparing a 6- versus a 3-layer cortex. These data provide one explanation for the great variability in tuber size and excitability seen in individuals with TSC.

In conclusion, we provide what we believe to be a novel strategy to generate cortical tuber-like lesions with features resembling TSC-associated lesions but without giant cells. Generating discrete cortical tuber-like lesions at a given location will allow us and others to uncover the mechanisms of lesion formation and identify new mTOR-associated targets to limit the formation of lesions and examine cortical excitability. Our strategy can also be applied to study other mTOR-associated pathologies or diseases such as polyhydramnios, megalencephaly, symptomatic epilepsy syndrome, fragile X syndrome, schizophrenia, and autism spectrum disorders

(58–62). The strategy described here can be used to increase mTOR activity in selective neuronal populations at a given time during embryonic development of *Tsc1*$^{fl/fl}$ mice. Such a strategy may help uncover alterations in the biochemistry and circuitry of TSC and other mTOR-associated neurodevelopmental disorders.

Methods

Animals. Research protocols were approved by the Yale University Institutional Animal Care and Use Committee. Experiments were performed on littermate mice obtained by crossing the following 2 lines of transgenic mice: *Tsc1*$^{fl/fl}$ (Jackson Laboratories) and *Tsc1*$^{WT/mut}$ (NCI). *Tsc1*$^{fl/fl}$ mice were from a mixed background (C57BL/6J, BALB/cJ, or 129/SvJae mice) and the genetic background of *Tsc1*$^{WT/mut}$ mice was B6;129S4. These 2 lines of mice were generated by David J. Kwiatkowski (Brigham and Women's Hospital, Harvard Medical School, Cambridge, Massachusetts, USA). The breeding lines were also crossed with the GFP fluorescent reporter line CAG-GFP (Jackson Laboratories; B6.Cg-Tg[CAG-Bgeo/GFP]21Lbe/J), in which, upon Cre expression, GFP is expressed. Mice were prescreened for successful electroporation prior to sacrificing by viewing with an epifluorescence microscope or a Kodak 4000 imager.

Genotyping. Tail or toe samples were prepared using standard protocols. We used previously published primers (17, 29). The primer combination allows for detection of the WT *Tsc1* allele at 295 bp, the floxed allele at 480 bp, and the mutant allele at 370 bp. The floxed allele contains the LoxP sites surrounding the sequence to be excised upon Cre recombination. The mutant allele lacks the sequence flanked by LoxP sites, thus making the hamartin protein non-functional.

In utero electroporation. DNA solution (~2 μg/μl) was diluted in PBS with 0.1% fast green as a tracer. DNA solution (0.1–0.5 μl) was injected into the lateral ventricle using a glass pipette in embryos at E15 or E16. After DNA injection using manual pressure, tweezer-type electrodes (model 520; BTX) were soaked in PBS and placed on the heads of the embryos, and three 25- to 50-V square pulses of 50 ms duration with 950-ms intervals were applied using a pulse generator (ECM830; BTX). A combination of 2 plasmids (p) encoding Cre:GFP (Cre fused to GFP) and mRFP under the chicken β-actin promoter with *CMV* enhancer (CAG), termed pCAG-cre:GFP and pCAG-mRFP (Addgene), were electroporated at E15–E16.5.

Slice preparation and immunostaining. P15 or P28 mice were deeply anesthetized with pentobarbital (50 mg/kg). P7 brains were also collected for testing for the presence of Cre and mRFP and a decrease in *Tsc1* using RT-PCR (Figure 1). The brain was then quickly removed and placed in 4% paraformaldehyde overnight at 4°C, then washed in 1× PBS. The region of electroporation was imaged using a Kodak 4000 imager. The next day, 100-μm-thick slices were prepared using a vibratome (Leica VTS 1000). Immunostaining was performed in free-floating 100-μm-thick slices as previously described (63). Free-floating sections were blocked in TBS containing 0.1% Triton X-100, 0.1% Tween-20, and 2% BSA and incubated in primary antibodies (see below) overnight at 4°C. After several washes in TBS containing 0.1% Tween-20, slices were incubated with the appropriate secondary antibody (Alexa Fluor series at 1:1,000 [Invitrogen]; or Cyanine series at 1:500 [Jackson ImmunoResearch]) for 1 hour at room temperature. Primary antibodies were rabbit anti-GFAP (1:1,000; Dako), goat anti-DCX (1:100; Santa Cruz Biotechnology Inc.), rabbit anti-hamartin (1:100; abcam; catalog no. ab32936), rabbit monoclonal anti-Ki67 (1:500; Vector Labs; VP-RM04), rabbit anti-pS6 (1:1,000; Cell Signaling; Ser240/244, 61H9, catalog no. 4838 for analysis and in the figures; S235/236, 2F9, catalog no. 4856, which displayed similar results as catalog no. 4838; data not shown), mouse anti-NeuN (1:500; Millipore), rabbit anti-GS (1:1,000; Sigma-Aldrich), and mouse anti-nestin (1:200, Rat-401; Developmental Studies Hybridoma Bank). Each staining was replicated at in least 4–5 slices from 3 different mice. Z-section images were acquired on a confocal microscope (Olympus FluoView 1000) with a ×20 dry objective (N.A. 0.75). Low-magnification images were acquired with a ×4 dry objective. Images were analyzed using Imaris 4.0 (Bitplane AG) and reconstructed using ImageJ 1.39t software (Wayne Rasband, NIH) or Photoshop CS3.

Microdissection, RNA extraction, and RT-PCR. Following fixation in 4% paraformaldehyde overnight at 4°C, the brains were rinsed in sterile 1× PBS overnight at 4°C. Rinsed brains were sectioned into 500-μm-thick coronal sections in sterile 1× PBS. Microdissection of tissues of interest was performed under an epifluorescence dissecting microscope. To lyse tissue and facilitate RNA isolation, the fixed tissue was incubated with proteinase K and digestion buffer for 30 minutes on the shaker (5,200 *g* and 55°C, as indicated by SABiosciences FFPE RNA extraction kit). Trizol reagent (750 μl) plus 200 μl of chloroform were added to 250 μl of digested sample and vortexed for 1 minute. Following centrifugation for 15 minutes at 4°C and 12,000 *g*, the top aqueous phase was transferred to a fresh reaction tube. After adding 1,000 μl of ethanol, the sample was vortexed for 1 minute, transferred to SABioscience spin columns, and centrifuged at 8,000 *g* for 15 seconds. The columns were rinsed with wash buffer and 75% ETOH. Following centrifugation, the RNA was eluted with RNase-free deionized H_2O prior to determining its concentration and purity on a spectrophotometer. The samples with contamination were subjected to an additional ethanol/sodium acetate precipitation.

For RT-PCR, 2.12 μg of RNA was mixed with dNTPs, random primers (Invitrogen), and RNase/DNase-free deionized H_2O, heated for 5 minutes at 65°C, and then rapidly chilled on wet ice for 5 minutes, followed by brief centrifugation. DTT, RNase out, and SuperScript III were then added to each sample and reverse transcribed in a BioRad MyCycler. cDNA was then subjected to PCR using primers to *Gapdh* and *Tsc1*. *Tsc1* primers were 5′-TCAAGCACCTCTTCTGCCTT-3′ and 5′-GTCACATGGCCTGGTTTCTT-3′.

Genomic and plasmid DNA isolation. Fresh, unfixed tissue was subjected to a proteinase K dilution and genomic DNA isolated using a DNeasy kit (DNA extraction). Quantification of DNA purity and concentration was performed, and approximately 0.19 μg of DNA was added to PCR reactions. Invitrogen 10× PCR buffer was added to 10 mM dNTP mix, 50 mM $MgSO_4$, autoclaved DNase-free deionized H_2O, and Platinum Taq. The reaction volume was 25 μl after adding 1 μl of each forward and reverse primer with 3 μl of the appropriate sample. PCR was performed in a Bio-Rad MyCycler (32–36 cycles). For plasmid and recombination detection, 5 μl of product was subjected to a second round of PCR. Amplicons were visualized by running samples diluted in 10× blue juice DNA loading buffer loaded onto a 2% agarose gel run at 100 V for 30 minutes alongside a 100-bp DNA ladder (Invitrogen). DNA primers for Cre and mRFP were as follows: (5′-GCAACGAGTGATGAGGTTCGCAAG-3′, 5′-TCCGCCGCATAACCAGTGAAACAG-3′ (307 bp), and 5′-TCTGGGCACAGTGACCTCAGTG-3′, 5′-GGGACATCTTCCCATTCTAAAC-3′ (352 bp).

qRT-PCR. mRNA transcripts were quantified by the standard curve method of qRT-PCR. cDNA from P28 cortical tissue was amplified with the specified primers and detected with SYBR Green (Bio-Rad) by a Chromogen-modified iCycler.

Layering, cell size, and pS6 immunostaining analyses. To analyze the laminar distribution of electroporated cells, images of mRFP$^+$ cell–containing coronal sections were acquired with a ×4 dry objective on a Fluoview 1000 Olympus confocal microscope. Using Image J v1.44c software, image thresholding was applied for mRFP; the resulting 8-bit image was subjected to binary watershedding to separate "clumped" cells from one another and projected onto the transmitted channels of the same image. Cortical layers were visualized using light microscopy and DAPI counterstaining and distinguished with anatomical landmarks (e.g., location of corpus callosum to find layer V/VI based on cell density, pial surface and marginal

zone to find layer II/III based on cell density). Each layer was identified as a region of interest (ROI) with the polygon tool. Cell counts were automated using the particle analyzer and to exclude debris and cell clumping we used the following settings (area, 0.005 cm^2 < 0.01 cm^2). Three sections were analyzed per mouse.

To measure cell size, Z-stack images of $mRFP^+$ cells, $NeuN^+$, or GS^+ cells in coronal sections were acquired with a ×20 dry objective (Numerical Aperture, 0.75) using high-low settings to minimize saturation. In Image J, the freehand tracing tool was used to outline cell somas. Cell size was represented relative to the indicated controls.

To measure mTOR activity, immunostaining was performed using an antibody to phosphorylated serine 240/244 of the S6 ribosomal protein (pS6). Serial Z-stacks were acquired under the same settings for the ipsilateral and contralateral hemispheres of coronal sections. Because layer II/III cortical neurons project to the contralateral hemisphere, $mRFP^+$ axons were followed to measure pS6 levels in cells of the non-electroporated region. ROIs were generated using an elliptical selection tool, and average intensities for each ROI were determined. The ROI did not include the nucleus that had low pS6 staining. For both cell size and pS6 staining measurement, 3 sections per mouse and 38–111 cells per section were analyzed.

Seizure test. Pentylenetetrazole (31.25 μg/g; Invitrogen) was administered via intraperitoneal injection at 10-minute intervals in mice electroporated at E15. The injections were given until the mice exhibited a generalized tonic-clonic seizure (3–4 injections). The time to onset of the generalized seizure was video-recorded. Observers were blinded to the genotypes of the mice and as to whether they were electroporated.

Statistics. Analysis of cell size and pS6 was performed on an average of 43 and 45 cells per slice, respectively, from 3–4 animals in each condition. Laminar distribution of cells was performed on 1–2 slices for 3–4 animals of each genotype. *t* tests were performed for each comparison made. PTZ-induced seizure assays were performed on 3–4 animals for each condition.

Acknowledgments

This work was supported by grants from the Department of Defense (to A. Bordey), a Tuberous Sclerosis Alliance fellowship (to J.-C. Platel), and a training grant from the Department of Neurobiology and an Epilepsy Foundation fellowship (to D.M. Feliciano).

Received for publication August 26, 2010, and accepted in revised form January 26, 2011.

Address correspondence to: Angélique Bordey, Department of Neurosurgery, Yale University School of Medicine, 333 Cedar Street, FMB 422, New Haven, Connecticut 06520-8082, USA. Phone: 203.737.2515; Fax: 203.737.2159; E-mail: angelique.bordey@yale.edu.

Jean-Claude Platel's current address is: University of Saarland, School of Medicine, Department of Physiology, Homburg/Saar, Germany.

1. Osborne JP, Fryer A, Webb D. Epidemiology of tuberous sclerosis. *Ann N Y Acad Sci*. 1991;615:125–127.
2. European Chromosome 16 Tuberous Sclerosis Consortium. Identification and characterization of the tuberous sclerosis gene on chromosome 16. *Cell*. 1993;75(7):1305–1315.
3. Curatolo P, Seri S, Verdecchia M, Bombardieri R. Infantile spasms in tuberous sclerosis complex. *Brain Dev*. 2001;23(7):502–507.
4. Holmes GL, Stafstrom CE. Tuberous sclerosis complex and epilepsy: recent developments and future challenges. *Epilepsia*. 2007;48(4):617–630.
5. Webb DW, Fryer AE, Osborne JP. Morbidity associated with tuberous sclerosis: a population study. *Dev Med Child Neurol*. 1996;38(2):146–155.
6. Weiner DM, Ewalt DH, Roach ES, Hensle TW. The tuberous sclerosis complex: a comprehensive review. *J Am Coll Surg*. 1998;187(5):548–561.
7. Thiele EA. Managing epilepsy in tuberous sclerosis complex. *J Child Neurol*. 2004;19(9):680–686.
8. Jansen FE, et al. Epilepsy surgery in tuberous sclerosis: the Dutch experience. *Seizure*. 2007;16(5):445–453.
9. Jansen FE, et al. Cognitive impairment in tuberous sclerosis complex is a multifactorial condition. *Neurology*. 2008;70(12):916–923.
10. Jansen FE. Introduction--epileptogenic cortical dysplasia: emerging trends in diagnosis, treatment, and pathogenesis. *Epilepsia*. 2009;50 suppl 9:1–2.
11. Kobayashi T, Hirayama Y, Kobayashi E, Kubo Y, Hino O. A germline insertion in the tuberous sclerosis (Tsc2) gene gives rise to the Eker rat model of dominantly inherited cancer. *Nat Genet*. 1995;9(1):70–74.
12. Mizuguchi M, Takashima S, Yamanouchi H, Nakazato Y, Mitani H, Hino O. Novel cerebral lesions in the Eker rat model of tuberous sclerosis: cortical tuber and anaplastic ganglioglioma. *J Neuropathol Exp Neurol*. 2000;59(3):188–196.
13. Eker R, Mossige J, Johannessen JV, Aars H. Hereditary renal adenomas and adenocarcinomas in rats. *Diagn Histopathol*. 1981;4(1):99–110.
14. Scheidenhelm DK, Gutmann DH. Mouse models of tuberous sclerosis complex. *J Child Neurol*. 2004; 19(9):726–733.
15. Piedimonte LR, Wailes IK, Weiner HL. Tuberous sclerosis complex: molecular pathogenesis and animal models. *Neurosurg Focus*. 2006;20(1):E4.
16. Uhlmann EJ, et al. Heterozygosity for the tuberous sclerosis complex (TSC) gene products results in increased astrocyte numbers and decreased p27-Kip1 expression in TSC2+/– cells. *Oncogene*. 2002; 21(25):4050–4059.
17. Kwiatkowski DJ, et al. A mouse model of TSC1 reveals sex-dependent lethality from liver hemangiomas, and up-regulation of p70S6 kinase activity in Tsc1 null cells. *Hum Mol Genet*. 2002;11(5):525–534.
18. Crino PB, Aronica E, Baltuch G, Nathanson KL. Biallelic TSC gene inactivation in tuberous sclerosis complex. *Neurology*. 2010;74(21):1716–1723.
19. Qin W, et al. Analysis of TSC cortical tubers by deep sequencing of TSC1, TSC2 and KRAS demonstrates that small second-hit mutations in these genes are rare events. *Brain Pathol*. 2010;20(6):1096–1105.
20. Wenzel HJ, Patel LS, Robbins CA, Emmi A, Yeung RS, Schwartzkroin PA. Morphology of cerebral lesions in the Eker rat model of tuberous sclerosis. *Acta Neuropathol*. 2004;108(2):97–108.
21. Uhlmann EJ, et al. Astrocyte-specific TSC1 conditional knockout mice exhibit abnormal neuronal organization and seizures. *Ann Neurol*. 2002;52(3):285–296.
22. Meikle L, et al. A mouse model of tuberous sclerosis: neuronal loss of Tsc1 causes dysplastic and ectopic neurons, reduced myelination, seizure activity, and limited survival. *J Neurosci*. 2007;27(21):5546–5558.
23. Way SW, McKenna J 3rd, Mietzsch U, Reith RM, Wu HC, Gambello MJ. Loss of Tsc2 in radial glia models the brain pathology of tuberous sclerosis complex in the mouse. *Hum Mol Genet*. 2009; 18(7):1252–1265.
24. Crino PB, Nathanson KL, Henske EP. The tuberous sclerosis complex. *N Engl J Med*. 2006; 355(13):1345–1356.
25. Richardson EP Jr. Pathology of tuberous sclerosis. Neuropathologic aspects. *Ann N Y Acad Sci*. 1991; 615:128–139.
26. Mizuguchi M. Abnormal giant cells in the cerebral lesions of tuberous sclerosis complex. *Congenit Anom (Kyoto)*. 2007;47(1):2–8.
27. Crino PB. Molecular pathogenesis of tuber formation in tuberous sclerosis complex. *J Child Neurol*. 2004; 19(9):716–725.
28. Mizuguchi M, Takashima S. Neuropathology of tuberous sclerosis. *Brain Dev*. 2001;23(7):508–515.
29. Meikle L, et al. A mouse model of cardiac rhabdomyoma generated by loss of Tsc1 in ventricular myocytes. *Hum Mol Genet*. 2005;14(3):429–435.
30. Takahashi T, Goto T, Miyama S, Nowakowski RS, Caviness VS Jr. Sequence of neuron origin and neocortical laminar fate: relation to cell cycle of origin in the developing murine cerebral wall. *J Neurosci*. 1999;19(23):10357–10371.
31. Lee DF, et al. IKK beta suppression of TSC1 links inflammation and tumor angiogenesis via the mTOR pathway. *Cell*. 2007;130(3):440–455.
32. Molyneaux BJ, Arlotta P, Menezes JR, Macklis JD. Neuronal subtype specification in the cerebral cortex. *Nat Rev Neurosci*. 2007;8(6):427–437.
33. Yamanouchi H, Jay V, Rutka JT, Takashima S, Becker LE. Evidence of abnormal differentiation in giant cells of tuberous sclerosis. *Pediatr Neurol*. 1997;17(1):49–53.
34. Sosunov AA, et al. Tuberous sclerosis: a primary pathology of astrocytes? *Epilepsia*. 2008; 49(suppl 2):53–62.
35. Eid T, Williamson A, Lee TS, Petroff OA, de Lanerolle NC. Glutamate and astrocytes--key players in human mesial temporal lobe epilepsy? *Epilepsia*. 2008;49(suppl 2):42–52.
36. Jansen LA, Uhlmann EJ, Crino PB, Gutmann DH, Wong M. Epileptogenesis and reduced inward rectifier potassium current in tuberous sclerosis complex-1-deficient astrocytes. *Epilepsia*. 2005; 46(12):1871–1880.
37. Baybis M, et al. mTOR cascade activation distinguishes tubers from focal cortical dysplasia. *Ann Neurol*. 2004;56(4):478–487.
38. Major P, et al. Are cortical tubers epileptogenic? Evidence from electrocorticography. *Epilepsia*. 2009; 50(1):147–154.
39. Cusmai R, Chiron C, Curatolo P, Dulac O, Tran-Dinh S. Topographic comparative study of magnetic resonance imaging and electroencephalography in 34 children with tuberous sclerosis. *Epilepsia*. 1990;31(6):747–755.
40. Chu-Shore CJ, Major P, Montenegro M, Thiele E. Cyst-like tubers are associated with TSC2 and epilepsy in tuberous sclerosis complex. *Neurology*. 2009; 72(13):1165–1169.
41. Boer K, et al. Clinicopathological and immunohisto-

chemical findings in an autopsy case of tuberous sclerosis complex. *Neuropathology*. 2008;28(6):577–590.
42. Ridler K, et al. Neuroanatomical correlates of memory deficits in tuberous sclerosis complex. *Cereb Cortex*. 2007;17(2):261–271.
43. Goorden SM, van Woerden GM, van der WL, Cheadle JP, Elgersma Y. Cognitive deficits in Tsc1+/– mice in the absence of cerebral lesions and seizures. *Ann Neurol*. 2007;62(6):648–655.
44. Ehninger D, et al. Reversal of learning deficits in a Tsc2+/– mouse model of tuberous sclerosis. *Nat Med*. 2008;14(8):843–848.
45. Hirose T, et al. Tuber and subependymal giant cell astrocytoma associated with tuberous sclerosis: an immunohistochemical, ultrastructural, and immunoelectron and microscopic study. *Acta Neuropathol*. 1995;90(4):387–399.
46. Thorp JA, O'Connor M, Jones AM, Hoffman EL, Belden B. Does perinatal phenobarbital exposure affect developmental outcome at age 2? *Am J Perinatol*. 1999;16(2):51–60.
47. Zeng LH, Rensing NR, Zhang B, Gutmann DH, Gambello MJ, Wong M. Tsc2 gene inactivation causes a more severe epilepsy phenotype than Tsc1 inactivation in a mouse model of Tuberous Sclerosis Complex. *Hum Mol Genet*. 2011;20(3):445–454.
48. Hansen DV, Lui JH, Parker PR, Kriegstein AR. Neurogenic radial glia in the outer subventricular zone of human neocortex. *Nature*. 2010;464(7288):554–561.
49. Smart IH, Dehay C, Giroud P, Berland M, Kennedy H. Unique morphological features of the proliferative zones and postmitotic compartments of the neural epithelium giving rise to striate and extrastriate cortex in the monkey. *Cereb Cortex*. 2002;12(1):37–53.
50. Wong M, et al. Impaired glial glutamate transport in a mouse tuberous sclerosis epilepsy model. *Ann Neurol*. 2003;54(2):251–256.
51. Zeng LH, et al. Abnormal glutamate homeostasis and impaired synaptic plasticity and learning in a mouse model of tuberous sclerosis complex. *Neurobiol Dis*. 2007;28(2):184–196.
52. Bordey A, Sontheimer H. Properties of human glial cells associated with epileptic seizure foci. *Epilepsy Res*. 1998;32(1–2):286–303.
53. Boer K, et al. Cellular localization of metabotropic glutamate receptors in cortical tubers and subependymal giant cell tumors of tuberous sclerosis complex. *NeuroScience*. 2008;156(1):203–215.
54. Yang L, et al. Astrocyte activation and memory impairment in the repetitive febrile seizures model. *Epilepsy Res*. 2009;86(2–3):209–220.
55. Kramer RH, Fortin DL, Trauner D. New photochemical tools for controlling neuronal activity. *Curr Opin Neurobiol*. 2009;19(5):544–552.
56. Alexander GM, et al. Remote control of neuronal activity in transgenic mice expressing evolved G protein-coupled receptors. *Neuron*. 2009;63(1):27–39.
57. Yeung RS. Tuberous sclerosis as an underlying basis for infantile spasm. *Int Rev Neurobiol*. 2002; 49:315–332.
58. Orlova KA, et al. STRADalpha deficiency results in aberrant mTORC1 signaling during corticogenesis in humans and mice. *J Clin Invest*. 2010; 120(5):1591–1602.
59. Chu TT, Liu Y, Kemether E. Thalamic transcriptome screening in three psychiatric states. *J Hum Genet*. 2009;54(11):665–675.
60. Sharma A, et al. Dysregulation of mTOR signaling in fragile X syndrome. *J Neurosci*. 2010;30(2):694–702.
61. Swiech L, Perycz M, Malik A, Jaworski J. Role of mTOR in physiology and pathology of the nervous system. *Biochim Biophys Acta*. 2008;1784(1):116–132.
62. Bourgeron T. A synaptic trek to autism. *Curr Opin Neurobiol*. 2009;19(2):231–234.
63. Platel JC, Gordon V, Heintz T, Bordey A. GFAP-GFP neural progenitors are antigenically homogeneous and anchored in their enclosed mosaic niche. *Glia*. 2009;57(1):66–78.